Astron. Astrophys. 355, 355–364 (2000)

ASTRONOMY AND ASTROPHYSICS

Small and large scale magnetic structures involved in the development of the 1992 October 28 solar flare

J.-P. Raulin[1], **N. Vilmer**[2], **G. Trottet**[2], **N. Nitta**[3], **A.V.R. Silva**[1], **P. Kaufmann**[1], **E. Correia**[1], **and A. Magun**[4]

[1] CRAAE/CRAAM, Instituto Presbiteriano Mackenzie, Rua da Consolação 896, 01302-907, São Paulo, Brazil (raulin@craae.mackenzie.br)
[2] DASOP, CNRS-URA 8046, Observatoire de Paris, Section de Meudon, 92195 Meudon, France
[3] Lockheed Martin Solar & Astrophysics Laboratory, Dep/L9-41, B/252, 3251 Hanover St., Palo Alto, CA 94304, USA
[4] Institute of Applied Physics, University of Bern, Sidlerstrasse 5, 3012 Bern, Switzerland

Received 7 July 1999 / Accepted 17 December 1999

Abstract. We report spatially resolved observations of a solar flare, obtained in a wide range of wavelengths including soft and hard X-rays, decimeter-meter and millimeter radio emissions. This unique combination of data (including the simultaneous fast localization of emission at millimeter wavelengths) allows us to conclude that, even if the 1992 October 28 flare is a moderate one in terms of the amount of energy contained in the thermal plasma and in non thermal electrons, the magnetic configuration involved in the flare development is complex at all spatial scales. Furthermore, it is shown that stepwise temporal evolutions of the amount of energy release in non thermal electrons are closely related to stepwise changes of the magnetic structures of all spatial scales illuminated either by hot plasma or by non-thermal electrons. This provides some evidence that different episodes of energy release are triggered by loop-loop interaction and that the site of particle acceleration changes rapidly within the energy release volume. These findings are discussed in the context of flare models as well as with respect to the fragmented nature of energy release in solar flares.

Key words: Sun: activity – Sun: flares – Sun: particle emission – Sun: radio radiation

1. Introduction

In early solar flare models the dissipation of magnetic energy was generally described in terms of formation of neutral current sheets, using observations mainly described in terms of single bipolar configurations (Sturrock 1966; Hirayama 1974; Kopp & Pneuman 1976). With the improvement of imaging capabilities in various wavelength domains, it became clear that the above view was oversimplified. For example, SMM solar flare observations showed that during the flare impulsive phase, strong electron acceleration and heating occur in two or more magnetic structures, providing observational support to the reconnection model proposed by Heyvaerts et al. (1977). Loop-loop interaction thus appeared as a fundamental ingredient to trigger the flare energy release (Hernandez et al. 1986; Machado et al. 1988). More recently, YOHKOH observations have provided further support to this interpretation (e.g. Hanaoka 1994; Inda-Koide 1994). Simultaneous soft X-ray (SXR), HXR and microwave observations of solar flares, have also led to the conclusion that during flares, coronal loops of different spatial scales are involved (Nishio et al. 1997; Hanaoka 1997). Combined observations of long duration flares at soft X-ray and decimeter-meter wavelengths have also provided evidence that large scale magnetic reconnection between active region loops and surrounding magnetic fields may occur together with similar interaction in the active region (Manoharan et al. 1996). However, such phenomena are found on timescales of a few hours, i.e. on much longer time scales than the flare impulsive phase.

Many combined HXR/gamma-ray spectral measurements and decimeter-meter radio imaging observations have shown that in the course of the flare development various large scale coronal structures are successively and/or simultaneously activated (see e.g. Trottet 1994 for a review). It was also found that the spectral characteristics of flare accelerated electrons as deduced from hard X-ray (HXR) observations evolve in the course of solar flares, in close temporal association with the "activation" (brightening) of these large scale magnetic structures revealed by radio emission of electrons accelerated simultaneously with X-ray emitting ones in the flare region (Raoult et al. 1985; Chupp et al. 1993; Trottet et al. 1994; Trottet et al. 1998). All these observations are important to probe the configuration of the global magnetic structures in which flare energy release occur and in which particles are accelerated and propagate. While the evolution of the active region magnetic field leading to flare energy release operates on magneto-hydrodynamic time scales many observations show that particle acceleration proceeds on much faster timescales. In particular, studies of fast time structures in millimeter waves (Kaufmann et al. 1980; Correia et al. 1995; Raulin et al. 1998) and also in HXR (Kiplinger 1983; Hurley et al. 1983, Aschwanden et al. 1995; Vilmer et al. 1995) have shown that non thermal energy release in flares may result from a succession of discrete accelerations occurring on subsecond time scales and characterized by different injections of non thermal electrons. The centroid positions of these fast time structures observed at millimeter wavelengths show vari-

Send offprint requests to: J.-P. Raulin

ations in space of a few arc seconds on time scales of a few seconds to a few tens of seconds (Corrreia et al. 1995). These changes of localization, sometimes spread over tens of arcseconds (Raulin et al. 1998), suggest that during the development of a solar burst, the successive episodes of electron acceleration occur in different very localized sites (i.e. different small scale magnetic structures) distributed over a large area of the active region magnetic field. These observations, which agree with earlier suggestions (Kaufmann 1985), provide support to the theoretical work designed to explore the physics of fragmented energy release and the development of "avalanche" models (Lu et al. 1993) or "statistical flare" models (Vlahos 1994). These models expect the flare released energy to be built up by thousands of small dissipations, each of them lasting a few hundred milliseconds and involving spatial scales smaller than one arcsecond.

In this paper we use a unique combination of spatially resolved observations obtained simultaneously in a wide range of wavelengths including HXR, SXR, decimeter-meter and millimeter emissions to investigate the evolution in time and space of the pattern of both large and small scale magnetic structures traced by the energetic electrons and by the thermal plasma. The results of the observations are discussed in the context of flare and energy release models.

2. Instrumentation

The imaging SXR and HXR observations were obtained respectively by the Soft X-ray Telescope (SXT)) and by the Hard X-ray Telescope (HXT) onboard the Yohkoh satellite. SXT provides full and partial disk images in the 0.25–4 keV energy range (Tsuneta et al. 1991). Images are taken through five different broad–band X-ray filters allowing the estimate of the isothermal temperatures and emission measures along the line of sight. Images can be obtained in quiet or flare mode, with different fields of view (FOV) and pixel resolution varying between $2.46''$ and $9.81''$. The fastest the images can be obtained is every 2 seconds. For the event studied in this paper, SXT observed AR 7321 in the quiet mode between 09:23:37 and 10:07:35 UT, and in the flare mode between 10:09:07 and 10:18:55 UT. HXT has a FOV of $35'$ by $35'$ and thus can detect HXR flare emission from the whole disk. Images are obtained in the 14–93 keV energy range, simultaneously in four energy bands, with a time resolution of 0.5 s, a spatial resolution of $5''$ (Kosugi et al. 1991) and an image synthesis FOV of $2.1'$ by $2.1'$.

HXR spectral data were taken from the Hard X-ray Spectrometer (HXS), which is part of the Wide Band Spectrometer (WBS) onboard the Yohkoh satellite. HXS provides 32 channel spectra in the 24–830 keV energy range with a time resolution of 1 s (Yoshimori et al. 1991).

The millimeter observations of the 1992 October 28 solar flare were obtained at 48 GHz by the 13.7 meter dish of the Itapetinga observatory, with a time resolution of 1 ms and a sensitivity of 0.04 sfu. The multiple receiver focal array produces five beams, with half power widths of $2'$, which partially overlap (Georges et al. 1989). The 1992 October 28 burst was observed in three of these beams. In principle, burst positions can be unambigously determined only when the event is detected in at least four beams (Herrmann et al. 1992; Costa et al. 1995; Giménez de Castro et al. 1999). We will show below that, for this event, the sizes of individual millimeter emitting sources are small compared to the Itapetinga beam size. Under these conditions, Giménez de Castro et al.(1999) have shown that measurements in three beams are sufficient to get estimates of: (i) the total flux density and (ii) the position of a single emitting source or the centroid position of multiple emitting sources. These data are complemented by total flux measurements at 3.1 and 5.2 GHz obtained with the Bern polarimeters with a time resolution of 1 s.

The decimetric–metric radio imaging observations were made with the Nançay Radioheliograph (NRH) (The Radioheliograph Group 1993). The data used here consist of East–West and North–South 1-D images of the solar brightness at 164 MHz, 236.6 MHz, 327 MHz, 408 MHz and 435 MHz. The time resolution is 1 s at all frequencies in both directions. The spatial resolution and the accuracy of absolute position measurements are inversely proportional to the observing frequency. During the 1992 October 28 event the spatial resolution (FWHM) and the accuracy of position measurements at 164 MHz were respectively $\sim 1'.4$ and $\sim 0'.2$ in the East–West direction and $\sim 4.4'$ and $\sim 0.6'$ in the North–South direction. Radio dynamic spectra of the Astrophysical Institute Potsdam in Tremsdorf have also been used for spectral identification of the decimetric–metric bursts (courtesy of Dr H. Aurass).

3. Observations

3.1. Temporal evolution of the flare

The 1992 October 28 Hα 1F (GOES C2.6) flare occurred in NOAA region 7321 (S24 W38). The GOES event started at $\sim$ 10:05:30 UT. The impulsive phase of this flare lasted untill $\sim$ 10:12 UT and was observed from the HXR domain (up to $\sim$ 200 keV) down to the dekametric radio domain. This impulsive phase emission was followed by type II and moving type IV radiation, observed at metric–dekametric radio wavelengths with no counterparts in the radio millimetric and HXR domains. The following analysis ignores this post-impulsive radio emission as well as the long-lasting SXR brightening in the late phase of the flare.

Fig. 1 shows the time evolution of the radio flux density at 164 MHz, 435 MHz (the two extreme NRH observing frequencies), at 5.2 GHZ and at 48 GHz together with the 14–23 keV count rate measured by the HXT low-channel and the 25–41 keV and 103–174 keV count rates measured by HXS. On the basis of the 103–174 keV time profile, the event has been divided into three time intervals, referred to as P1, P2 and P3 on Fig. 1:

- **P1: $\sim$ 10:07–10:08:45 UT**
  P1 roughly begins with the start of the 14–23 keV X-ray emission and lasts until the rise of higher energy HXR emission. It is characterized by a slow rise of the metric radio

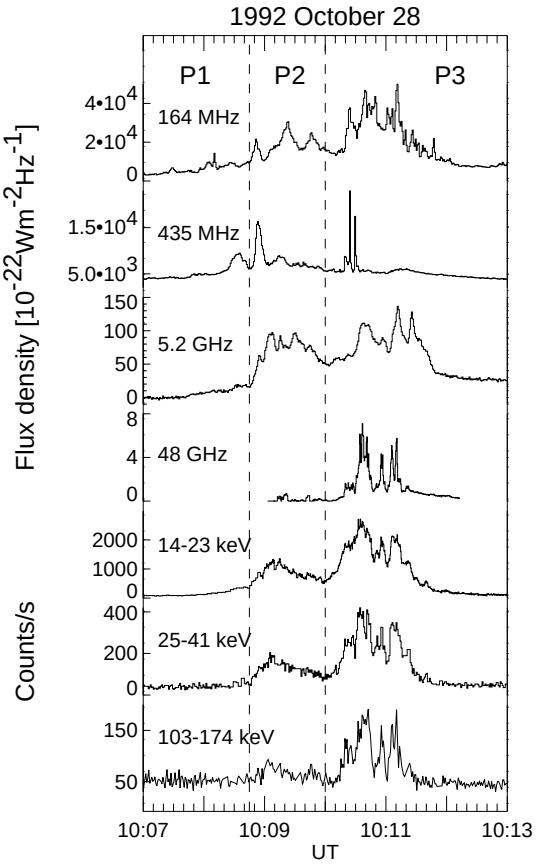

Fig. 1. Temporal evolution of the 1992 October 28 flare observed at different wavelengths. From top to bottom: radio flux density observed at 164 and 435 MHz by the NRH, at 5.2 GHz by the Bern polarimeters and at 48 GHz by the Itapetinga telescope; X-ray count rates measured in the low energy channel of Yohkoh/HXT and in two energy bands of Yohkoh/WBS. The vertical dashed lines show the starting time of P1, P2 and P3.

emission which is similar to that of the 5.2 GHz flux density and that of the 14–23 keV X-rays. During P1 as well as during the subsequent time intervals P2 and P3, the metric radio emission comprises continuum and short burst emission, some of which have been identified as type III bursts on spectral records. During P1, both the continuum and the superposed bursts show low frequency cutoffs around 150 MHz. No 48 GHz emission and no significant > 25 keV X-ray emission are detected, as usually observed during the pre-flash phase of a flare (e.g. Benz et al. 1983; Raoult et al. 1985).

- **P2: $\sim$ 10:08:45–10:10 UT**
  The beginning of P2 is characterized by a sudden increase of the HXR emission which is significantly detected up to $\sim$ 170 keV and of the 3.1 and 5.2 GHz flux densities. A faint (< 0.7 s.f.u) emission is also detected at 48 GHz, starting at 10:09:12 UT, i.e. during the maximum of the > 25 keV HXR emission. P2 is also clearly seen in the metric radio domain and starts with a group of type III bursts. The most striking feature is that at the beginning of P2 the low frequency cutoff of both the continuum and burst emission is suddenly shifted towards lower frequencies (< 100 MHz).

Table 1. Number of electrons above 20 keV (60 keV) and corresponding energies, derived from the spectral analysis of HXS data.

	P2	P3
e^- above 20 keV	$3.0\ 10^{36}$	$7.2\ 10^{36}$
e^- above 60 keV	$1.2\ 10^{34}$	$2.0\ 10^{34}$
ε in $e^- > 20$ keV (ergs)	$1.4\ 10^{29}$	$3.6\ 10^{29}$
ε in $e^- > 60$ keV (ergs)	$1.4\ 10^{27}$	$3.6\ 10^{27}$

- **P3: 10:10– $\sim$ 10:11:40 UT**
  P3 corresponds to a second and more intense increase of the emission at all wavelengths. Compared to P2, the HXR emission is about two times more intense at all energies and the 48 GHz emission is multiplied by ~ 10. The continuum and burst emissions are observed in the same spectral range as during P2 but P3 corresponds to a new sudden and simultaneous increase of the emission in the whole 450-100 MHz frequency range. The start of P3 is also marked by the occurrence of bright type III bursts at 435 MHz (see Fig. 1 from 10:10:20 to 10:10:30 UT).

The metric radio emission is caused by non-thermal electrons which radiate collectively. While type III bursts are a signature of electron beams moving upward through the corona, it is generally believed that the continuum emission is produced by electrons trapped in coronal loops. As most of the metric/decimetric emission observed is a continuum emission, we therefore conclude that:

- Electrons are accelerated during the whole impulsive phase of the flare, including during P1, where no > 25 keV HXR and no 48 GHz emission is detected. The observation of decimetric-metric as well as 3.1 and 5.2 GHz radio emission since the very beginning of P1, indicates that energetic electrons interact in both the upper and lower corona during the whole event.
- P1, P2 and P3 correspond to three successive episodes of acceleration of increasing efficiency (see the X-ray time profiles in Fig. 1 and the numbers in Table 1).
- At the transition from P1 to P2, the low frequency cutoff of the radio emission shifts towards lower frequencies (from 150 MHz to < 100 MHz). Though type III and continuum emission are radiated by different mechanisms, for a given observing frequency they are emitted close to the local plasma frequency (fundamental emission) or its first harmonic. The shift of the low frequency cutoff thus indicates that electrons have access to lower density magnetic structures during P2 and P3 than during P1 (density of $\sim 10^8$ cm^{-3} for P2 and P3; resp. $\sim 3\ 10^8$ cm^{-3} for P1, for fundamental emision).

3.2. SXR imaging observations

Fig. 2 displays the first available images after the beginning of P1 (top), P2 (middle) and P3 (bottom) taken with the Al.1 filter,

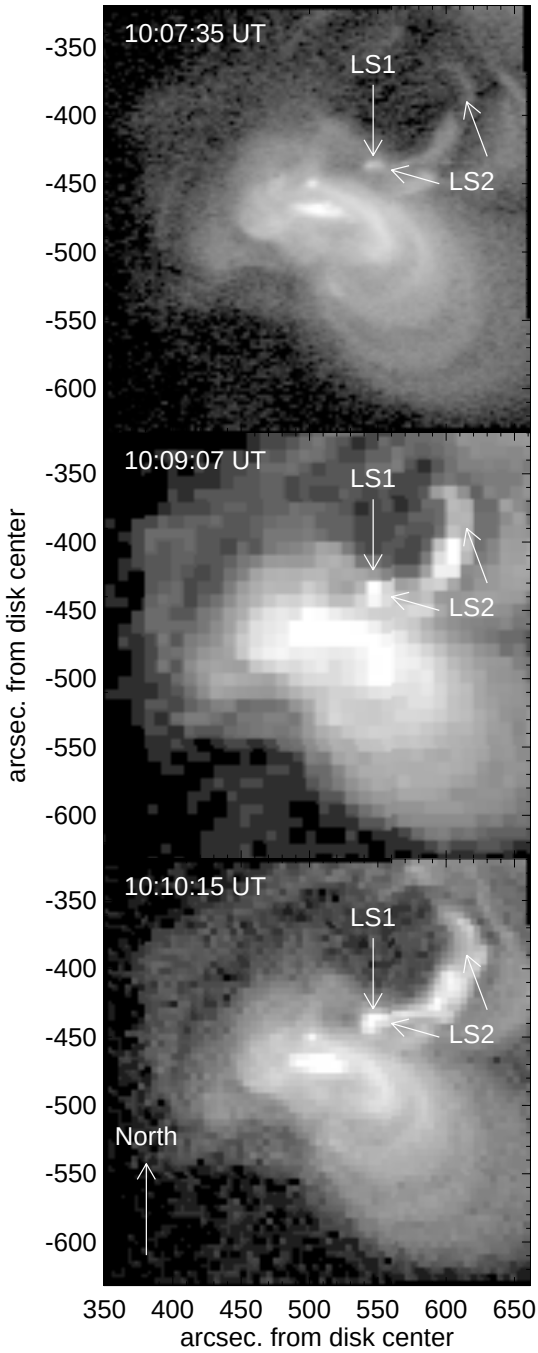

Fig. 2. SXT (Al.1 filter) images of AR 7321. The arrow shows the region LS1 and indicate the extension of the region LS2.

with 2.46″ (top), 9.81″ (middle) and 4.92″ (bottom) spatial resolution. Fig. 2 shows that the bulk of the SXT emission arises from a bright region at the center of each image and from two regions marked LS1 and LS2. The examination of all SXT images recorded during the 1992 October 28 event and the superposition of the SXR bright regions over photospheric magnetograms recorded on 1992 October 28 at 22:00 UT (Mees Solar Observatory, courtesy of T. Metcalf) and on 1992 October 29 at 19:32 UT (Kitt Peak Observatory, courtesy of NOAO), leads to the following statements:

– The bright SXT emission at the center of each image shown in Fig. 2 overlies the main magnetic inversion line within AR 7321. It thus arises from loop systems interconnecting the main active region magnetic polarities. A detailed analysis of the intensity time profile obtained with different filters, shows that the SXR emission of this ensemble of loops varies smoothly during the flare, starting to increase between 10:06:30 and 10:07:30 UT and reaching a maximum at 10:14:20 UT. Between 10:07 and 10:10 UT, there is only a slight increase of the intensity which results from an increase of the emission measure from 4.5 10^{47} cm^{-3} to 6 10^{47} cm^{-3}. Throughout the same time period the temperature remained roughtly constant at $\sim$ 8 MK.
– The region marked LS1 in Fig. 2 overlies a short magnetic inversion line at the NW border of AR 7321, and is located in projection onto the solar disk over the penumbra of a large sunspot observed in white-light images. LS1 appears thus as a compact ($\sim 20''$) system of loops, which begins to brighten between 10:06:30 and 10:07:30 UT, i.e. in association with the beginning of P1.
– The region marked LS2 in Fig. 2 has a loop-like shape which is more extended ($\sim 100''$) than LS1 and is elongated along the SE – NW direction. The SE foot point of the LS2 system is adjacent with LS1. An intensity increase of the NW part of LS2 is first observed between 10:08:35 and 10:09:07 UT, i.e. in association with the beginning of P2.
– The brightening expands along LS2 and reaches its SE extremity between 10:09:07 and 10:10:20 UT, i.e. in association with the beginning of P3. The long-lasting brightening of LS2 which is associated with the late phase of the flare (after P3) will not be discussed here.

The smallest field of view of flare mode SXT images covers the whole LS1 region but only the SE part of LS2. Using the complete sequence of flare mode images made with different filters, we have determined the temporal evolution of the emission measure (EM) and of the temperature (T) of LS1. The results are shown in Fig. 3, where the dashed vertical lines indicate the starting times of P1, P2 and P3. The examination of Fig. 3 leads to the following comments:

– The intensity of LS1, measured by the Al.1 filter, slightly increases by a factor of $\sim$ 1.5 during P1 and P2. This is due to an increase of both T from 5.5 $\pm$ 0.5 MK to 7.5 $\pm$ 0.5 MK and EM from $\sim$ 2.5 10^{46} cm^{-3} to $\sim$ 5 10^{46} cm^{-3}.
– During P3, T ($\approx$ 7.5 MK) remains constant untill $\sim$ 10:11 UT and then decreases. The strong enhancement of the intensity of LS1 is then due to that of EM alone, which reaches a maximum of 1.8 10^{47} cm^{-3} at $\sim$ 10:10:40 UT. SXT flare mode images indicate that the projected area of LS1 on the solar disk does not change significantly during the flare. This strongly suggests that the increase of EM is due to that of the electron density within LS1. The volume V of LS1 can be written as: $V = A^{3/2} = 1.9\ 10^{27}$ cm^3 where A is the area of LS1 measured on SXT images. The thermal energy contained in LS1 at 10:10:40 UT is then $W \simeq 2.5\ 10^{29}$ ergs.

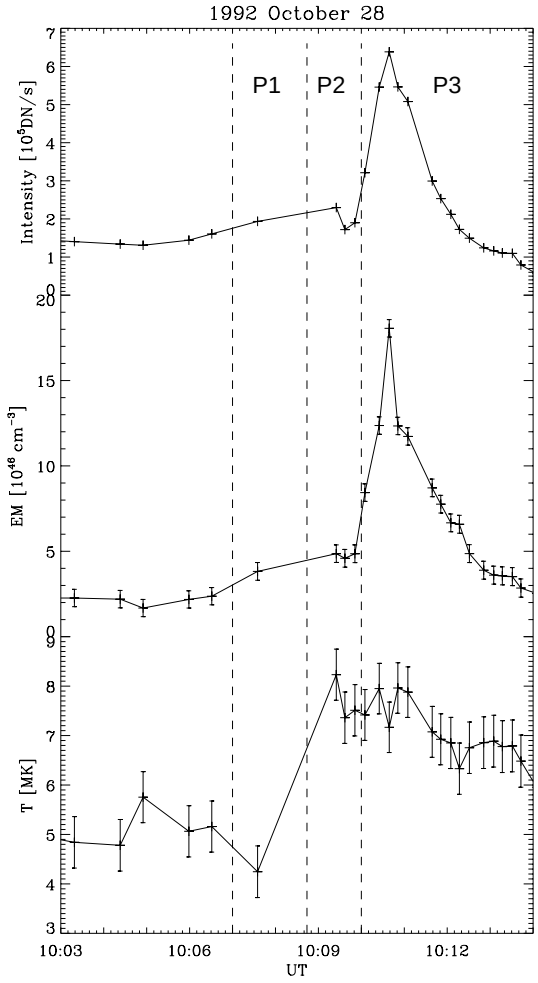

Fig. 3. From top to bottom: temporal evolution of the SXR intensity (Al.1 filter), of the emission measure (EM) and of the temperature (Te) for LS1 region.

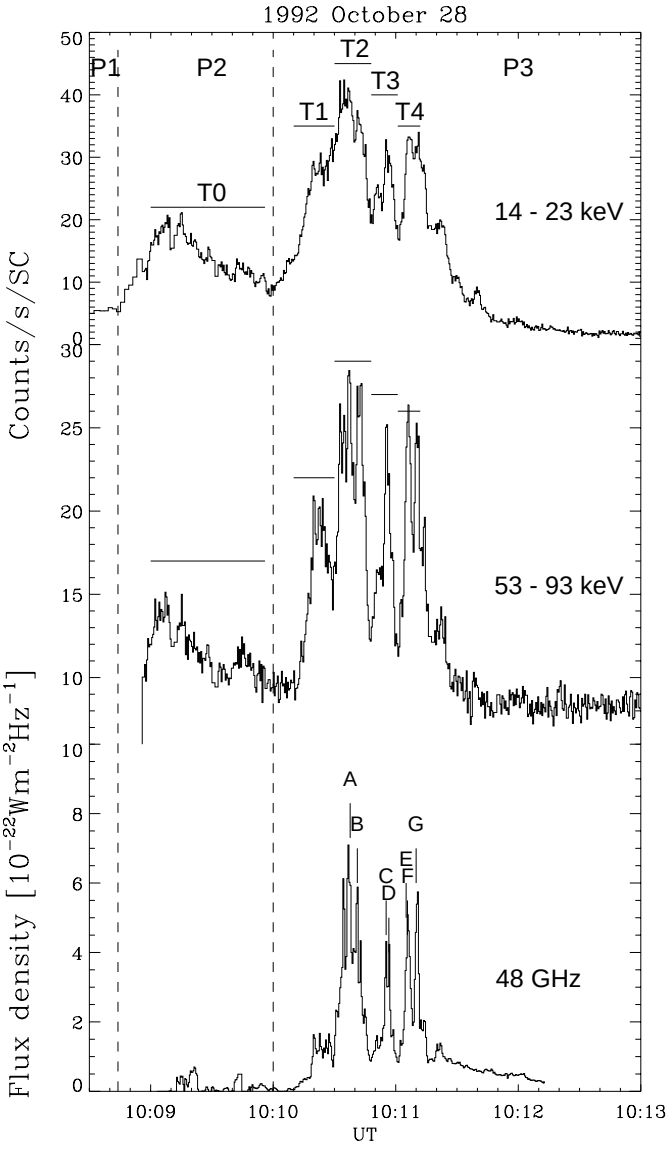

Fig. 4. Expanded view of the temporal evolution of the HXR emission count rate per subcollimator (14-23 keV and 53-93 keV) and of the radio flux density at 48 GHz. Thick horizontal bars show time intervals (T0-T4) during which HXR contour maps have been computed. The letters A-G in the 48 GHz time profile note different temporal fast structures.

3.3. HXR imaging and 48 GHz observations

Fig. 4 shows the temporal evolution of the 14–23 keV, 53–93 keV and 48 GHz emissions with an integration time of 0.5 s. During P3, there is a close similarity between the HXR time profiles at all energies and the 48 GHz one. In particular there is a one to one correspondance between HXR and millimeter time structures, some of which are labelled A–G.

The horizontal lines, marked T0 during P2 and T1, T2, T3 and T4 during P3 in Fig. 4, indicate the time intervals used to compute HXT maps. These maps which are shown for the 33–53 keV (right column) and 53–93 keV (left column) channels in Fig. 5, have been obtained by using the Maximum Entropy Method (Sakao 1994), with improved modulation patterns and algorithm (Sato et al. 1999). The center of each map has been chosen so that the FOV covers both LS1 and LS2 regions. In each frame the gray patches show the HXR image observed during T0, i.e. during P2. In order to compare the HXR emission from map to map, we have used the same contour levels for all maps.

Fig. 5 shows that the brightest HXR emission arises from a single and rather compact ($\sim 10''$) source, spatially associated with LS1. As the HXR source extent is only $\sim$ 4 x 4 HXT pixels, we consider that the double peaked source structure seen during T2 and T4 (53–93 keV maps) and during T1 (33–53 keV maps) is not real. This HXR source may thus be interpreted as a compact loop system, part of the LS1 complex, the foot points of which are not resolved by HXT. This flare thus belongs to ~ 30 % of the events observed with YOHKOH/HXT which are reported as single sources by Sakao (1994). In addition, during T1 (beginning of P3) there is a faint HXR source located near the northern extremity of LS2.

As was said in Sect. 2, the 1992 October 28 flare was observed with only three beams of the Itapetinga radio telescope. In this case, positions can only be computed if it is assumed

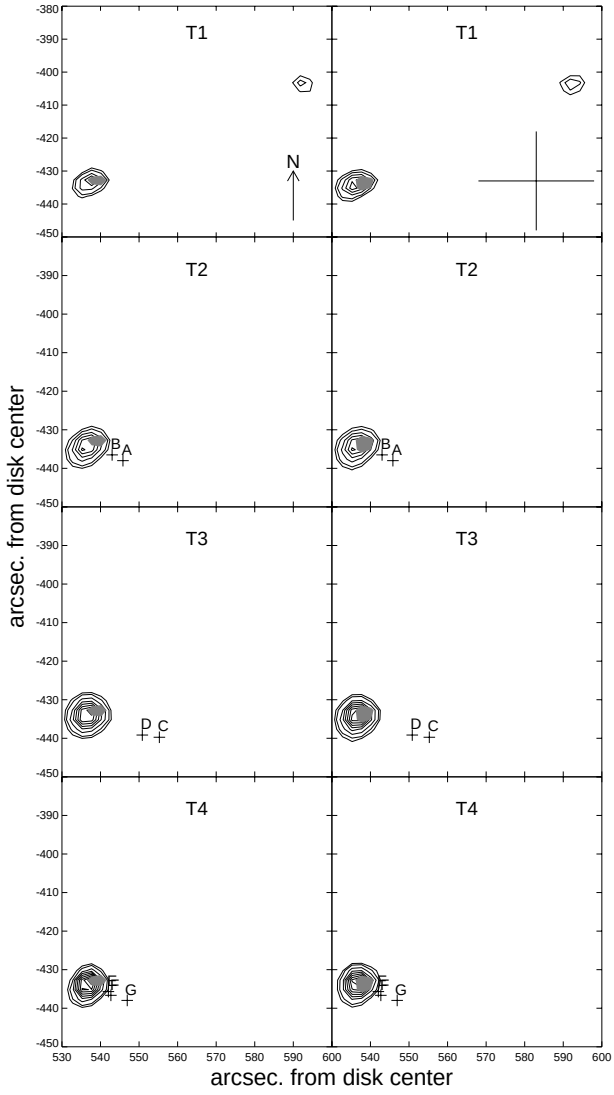

Fig. 5. Contours of equal intensity of the HXR emission observed during T1–T4, in the 53–93 keV (left column) and 33–53 keV (right column) channels. Contour levels are 0.15, 0.2, 0.3, 0.4, 0.5, 0.6, 0.7, 0.8, 0.9 and 0.99 of the maximum emission detected during time periods T1 to T4. The gray patches show the HXR emission observed during the phase P2 (T0). The crosses A–G show the position of the 48 GHz radio pulses observed during T2, T3 and T4. The small (big) cross sizes represent the accuracy of the relative (absolute) position of the radio pulses A–G.

that the 48 GHz emission arises from a source of small extent compared to the beam size. Giménez de Castro et al. (1999), have defined a contrast $K(t)$ computed from the antenna temperatures observed in different beams at each instant t and a minimum contrast K_{min} determined by the geometrical beam disposition at the time of the observation. They show that when $K(t) > K_{min}$ the extent of the emitting source is small compared to the beam size so that the position of the 48 GHz emitting source can be unambiguously determined. During the 1992 October 28 event, the condition $K(t) > K_{min}$ is verified over the time intervals T2, T3 and T4 which cover the bursts labelled A–G in Fig. 4. The accuracy on the absolute positions of the emitting sources, which depends upon various factors (see Costa et al. 1995), is estimated to be $\sim 15''$ for the present event. As the 1992 October 28 observations were performed during clear sky conditions, the accuracy on the relative positions of different emitting source, is given by that of the tracking system, i.e. $\pm$ 1.5″ r.m.s.

The centroid positions of the burst at 48 GHz are shown in Fig. 5 with cross symbols. For each individual burst, the position shown is a mean value computed during roughly $\pm$100 milliseconds around its peak. The size of the crosses gives the accuracy on the relative positions of bursts ($\pm 1.5''$). The precision on the absolute position, $\pm$ 15″, is indicated by a cross in the upper-right frame. Within these uncertainties, Fig. 5 suggests that the 48 GHz and the HXR emission arise from the same loop system (LS1). Any significant 48 GHz emission spatially associated with the northern foot point of LS2, during time periods T2, T3, T4 is unlikely. This is consistent with the fact that the magnetic field in the LS1 region is much higher than at the northern footpoint of LS2 where no significant magnetic feature is observed.

Fig. 5 also shows that the different radio bursts observed at 48 GHz during T2, T3 and T4, are displaced from each other by more than the accuracy of the burst relative positioning. For example C,D, during T3 are well separated from A,B and E–G occuring respectively during T2 and T4. Moreover, during each of the time interval T2–T4, individual radio bursts appearing sometimes within less than 2 seconds, are found to be located at significantly (a few arcseconds) different positions. For example this is the case for A and B during T2, C and D during T3, and E–F and G during T4. An earlier analysis of the same event by Correia et al. (1995), with the assumption of point-like emitting sources, led to similar results. They indeed reported relative burst positions consistent with those obtained here, however, they did not provide any estimate of the absolute burst position. It must finally be noticed that the displacement by a few arcseconds of the different radio bursts observed at 48 GHz on timescales less than 2 seconds is not contradictory to the observation that there is no substantial displacement of the HXR source for this moderate flare. Indeed, probably due to the imaging capability and also to count statistics, only displacement or separation with time on spatial scales of the order of 15 to 30 arcseconds have been reported for relatively large flares for the positions of HXR sources observed with YOHKOH/HXT (Sakao 1994).

3.4. HXR spectral analysis

A spectral analysis of the HXS data has been performed for count-rate spectra accumulated over 10 s between 10:09 UT and 10:11:20 UT. Within HXS sensitivity, no significant signal (3 σ above the background) was detected above 180 keV. For most of the event, the HXR photon spectrum is well represented by a double power law with a roughly constant break energy, E_b $\sim$ 60 keV. The spectral index below E_b, $\gamma_1 \approx 2.9 \pm 0.3$, remains constant through the whole period of analysis. The spectral in-

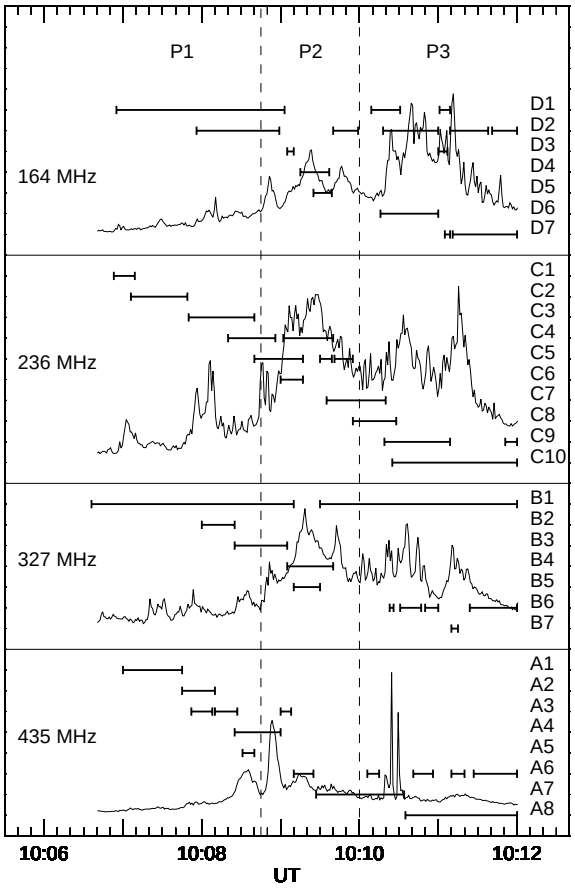

Fig. 6. Time of appearance and duration of decimeter-meter radio sources observed at different locations at each NRH observing frequency (thick horizontal lines), superimposed on the flux density time profiles

dex γ_2 above E_b is about 5 ± 0.5 up to 10:09:54 UT (during P2) and about 4.1 ± 0.2 after 10:10:14 UT, i.e.during P3. The values of the photon spectra deduced for the different peaks of the event from the spectral analysis of HXS observations are found to be consistent with spectra deduced from HXT observations at least in the last two channels of HXT falling in the HXS energy band (i.e. above 30 keV). As a first approximation, we have used the spectral parameters below or above E_b and thick target calculations by Brown (1971), in order to compute the number of interacting electrons above 20 and 60 keV during P2 and P3, as well as the total energy contained in these electrons. These numbers are indicated in Table 1. It should be noted that the energy deposited by > 20 keV electrons from the beginning of P3 untill 10:10:40 UT (time of the maximum of EM in LS1) is $\approx 1.4\ 10^{29}$ ergs. Though no spectral analysis was possible during P1, it is obvious that the number of and energy content in > 20 keV electrons are much smaller than during P2 and P3. We thus conclude that P1, P2 and P3 correspond to three successive episodes of acceleration of increasing efficiency. As shown in Crosby et al. (1993) the energy content in flare accelerated electrons above 20 keV lies in the range $\sim 10^{28}$–10^{32} ergs. The values reported in Table 1 indicate then that the 1992 October 28 appears as a rather moderate HXR flare.

3.5. Spatially resolved metric/decimetric observations

A detailed analysis of the spatial distribution of the different radio emitting sources has been performed for each NRH observing frequency. The results are summarized in Fig. 6, which, for each NRH observing frequency, shows together with the flux density time profile, the time of appearance and the duration of spatially distinct sources (labelled A1-A8, B1-B7, C1-C10,D1-D7; the results obtained at 435 MHz and 408 MHz being similar, the latter have not been reported in Fig. 6). In contrast to the HXR emission which mainly shows a single compact source, the metric radio emission at each NRH frequency arises from different sources at different locations and the spatial distribution of these sources strongly varies with time. Though new emitting sources switch on during P1, P2 and P3 there is no clear correspondance between the start of a new emitting source and the transition from P1 to P2 or from P2 to P3.

Fig. 7 shows the region covered by the ensemble of sources for each NRH observing frequency overlaid on a full-disk SXT image recorded at 10:07:25 UT. The general spatial pattern of the radio emission has a similar orientation as the one of the complex SXR emission that connects the flaring site in NOAA region 7321 (S24 W38) to a remote active region (NOAA region 7316 at S13 W59). This large scale organization of the metric radio sources indicates that the emission is most probably generated in a large-scale system of loops which interconnects the flare site with NOAA region 7316. The complex spatial distribution of the radio emitting sources and their time variations reveal that this large scale loop system is highly inhomogeneous and that within this complex of structures, electron trajectories change with time.

4. Discussion

This study of the 1992 October 28 flare is based on a unique combination of data providing spatially resolved observations in a wide wavelength range including HXR, SXR, radio decimeter-meter and also millimeter emissions. The results of the analysis are summarized below:

4.1. Evolution of the magnetic structures involved in the flare development

Based on the 103-174 keV HXR time profile, the impulsive phase of the 1992 October 28 flare consists in three successive episodes of electron acceleration (P1, P2, P3) which correspond to stepwise increases of the number and energy content of > 20 keV electrons. SXR imaging observations reveal that P1, P2 and P3 switch on when the brightness of the global magnetic structure (in particular LS1 and LS2) involved in the flare development suddenly changes at specific locations. This shows, in agreement with previous results (see e.g. Trottet 1994), that sudden changes in the magnetic pattern traced by energy release

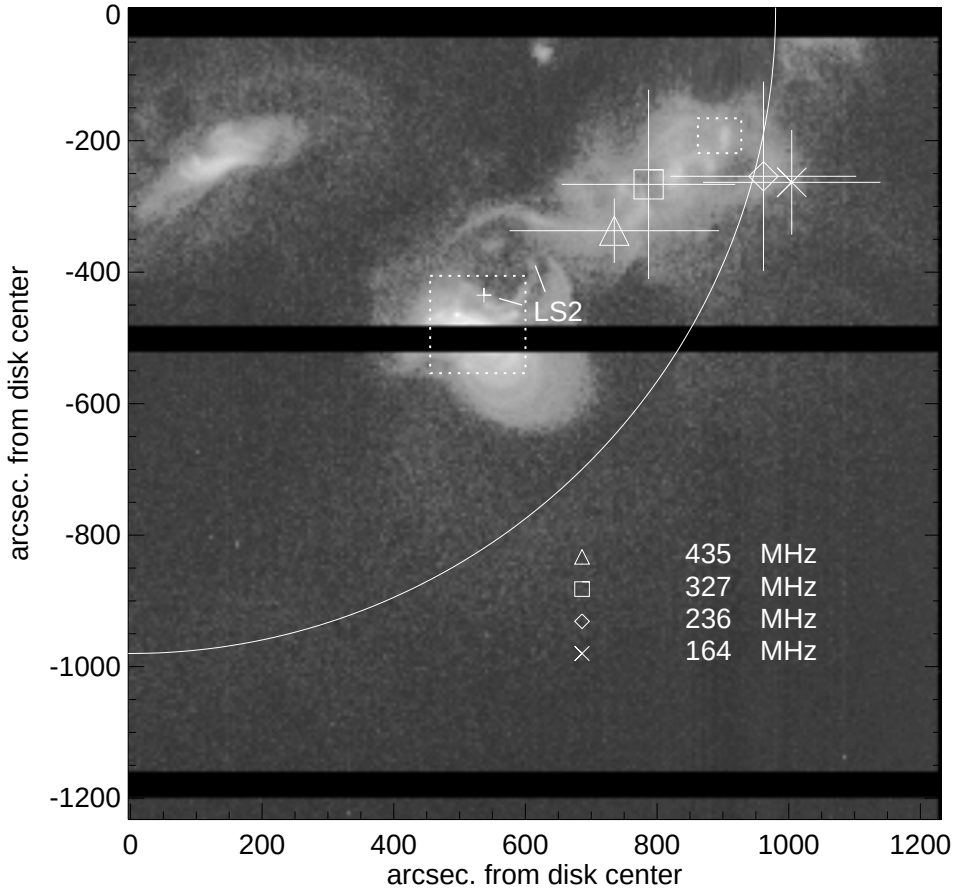

Fig. 7. Decimeter-meter burst positions during P1, P2 and P3, superimposed on a SXR image taken at 10:07:25 UT. The crosses show the EW and NS extensions of the region covered by the ensemble of emitting sources observed at each NRH frequency. Dotted boxes show, from bottom to top, the position of optical active regions, AR 7321 and AR 7316. The small cross shows the location of the LS1 loop system.

play a determining role in the efficiency of particle acceleration. The following flare scenario can be derived from the observations:

– Before the start of P1 the SXR emission consists of a complex of loops overlying the main magnetic inversion line of AR 7321. Because its emission varies smoothly during the flare, this loop system does not play a dominant part in the flare energy release and particle acceleration.
– The initial energy release (P1) occurs in a small and compact loop system (LS1). This may be due either to an increased magnetic shear of LS1 or to the interaction of LS1 with the more extended loop system (LS2). The lack of LS2 brightening during P1 is in favor of the former case. Indeed for the latter case, the most probable interaction region is located at the southern end of LS2 where the two loop systems LS1 and LS2 seem to connect each other and energy release is expected to be detected in both LS1 and LS2. During this initial period, microwave (3.1 and 5.2 GHz) and decimetric-metric observations show that non-thermal electrons are accelerated and have access to coronal magnetic structures of various spatial scales. However, the number of accelerated electrons is not sufficient to produce significant HXR emission above 25 keV with the HXS sensitivity.
– The second episode of energy release and particle acceleration (P2) starts when the NW extremity of LS2 suddenly brightens and the temperature of LS2 begins to rise. This is accompanied by an increase in the number of and energy contained in electrons above 20 keV which radiate at all wavelengths, i.e. by an increased efficiency of particle acceleration. HXR images show that the non-thermal bremsstrahlung interactions essentially occur in the LS1 region. The increased energy release in LS1 and the fact that energy is also released in LS2 probably results from interactions between loop systems LS1 and LS2. The brightening of the NW extremity of LS2 also suggests an interaction of LS2 with a loop system located north of it, since this brightening is very close to a dark region in the SXT images taken during P1 (see Fig. 2). This brightening probably corresponds to some foot points of LS2 where a HXR emitting source is observed at the beginning of P3. It is worthwhile noting that during P2, the brightening first observed in the NW part of LS2 extends towards LS1 at a speed close to 500 kms^{-1}. This is consistent with a perturbation, for example a heat conduction front, which moves along LS2 towards LS1.
– The onset of the last and strongest episode of energy release (P3) coincides with the arrival at LS1 of the perturbation (e.g. heat conduction front) initiated at the NW extremity of LS2 at the beginning of P2. Though it cannot be demonstrated by the available observations, a possible explanation is that a new magnetic field rearrangement (in the LS1-LS2 interaction region) leading to more efficient energy release

and particle acceleration is triggered by the arrival at LS1 of the perturbation. This is supported by the observation of a faint HXR source detected at the NW extremity of LS2 at the beginning of P3 (during time interval T1) which is the signature of the injection of a small fraction of the accelerated electrons in LS2. As shown in Sect. 3.2, the intense brightening of LS1 during P3 is essentially due to the increase of the electronic density of the thermal plasma contained in this loop system and the thermal energy W contained in LS1 at 10:10:40 UT $W \simeq 2.5\ 10^{29}$ ergs is comparable to the energy W_e deposited by the non thermal electrons in the upper chromosphere $W_e \simeq 1.4\ 10^{29}$ ergs. This suggests that the intense brightening of LS1 during P3 is the response of the loop system to the new non-thermal energy input triggered by the arrival at LS1 of the perturbation: the chromospheric gas, heated by non-thermal electrons (e.g. Fisher et al. 1985; Doschek et al. 1986; Fisher 1989), evaporates and gradually fills the LS1 loop system up to 10:10:40 UT and the thermal energy W contained in LS1 at 10:10:40 UT is comparable to the energy W_e deposited by the accelerated electrons (Doschek et al. 1986; Doschek 1990; Antonucci 1994). The short rise time of the emission measure is also consistent with an evaporation at a speed between 100 and 200 kms^{-1} in LS1 if a simple model such as the one described in Doschek et al. (1986) is used. Such a speed is in agreement with that of observed upflows (see e.g. Antonucci et al. 1999 for a review).

4.2. Energy release and acceleration processes

The analysis of the spatial and temporal evolution of the radio emission produced by the non-thermal electrons provide information on the evolution in time and space of the large and small scale magnetic structures traced by the energetic electrons.

– The similarity of the HXR and millimeter wave time profiles indicates a common origin of the emitting electrons. Although the positions of individual 48 GHz bursts are multiple and well separated in space and time, the shape and position of the X-ray loop system LS1 does not significantly vary. The lack of any measurable shift of the HXR source is not inconsistent with the observations at 48 GHz. Indeed, the spatial resolution of the HXT instrument as well as some potential limitation in count statistics does not allow to detect movements of the sources on spatial scales of a few arc seconds and time scales of a few seconds. Furthermore, the different emission mechanisms imply that the brightness of the emission is sensitive to different plasma parameters (density in the case of X-rays, magnetic fields and energetic electrons velocity distributions in the case of millimeter waves). The millimeter observations thus indicate that LS1 is quite inhomogeneous in terms of magnetic field strengths and that electron propagation paths from the acceleration region to the radiation site change with time on timescales much shorter than characteristic magnetohydrodynamic ones unless the involved spatial scales are much smaller than the observed ones. The most simple interpretation is then that displacements of the millimeter source reflect changes of the location(s) of the acceleration site(s) within the energy release volume.
– The time evolution of the decimetric-metric radio emission is also globally similar to that of the HXR, microwave and millimeter wave emissions on time scales of tens of seconds (see Fig. 1). Moreover the decimetric-metric radio sources have been found to be located in a large-scale (a few 10^5 km) highly inhomogeneous system of loops interconnecting the flaring site to a remote active region (see Sect. 3.5). These two facts support the idea that electrons radiating at all wavelengths are produced in the same acceleration region from which they are injected in both small scale and large scale loops (e.g. Trottet 1986). In this context, the presence of a large scale system of loops connecting two active regions does not appear as a necessary ingredient for the flare occurrence, it simply enables accelerated electrons to have access to the upper corona. The rapid changes of the spatial distribution of the decimetric-metric radio sources indicate that within the large scale loop system the flux tubes along which electrons propagate from the acceleration region to the upper corona also rapidly change with time. These changes occur on time scales much shorter than particle drift times across the magnetic field and far shorter than time scales inferred for large-scale reconnection processes (see e.g. Manoharan et al. 1996). As in the case of the millimeter emission, this strongly suggests that the location of the acceleration site within the energy release volume changes rapidly with time. However, there is no obvious relationship between the switch on of new millimeter sources and new decimetric-metric sources. This is expected if for a given location of the acceleration site, electrons get preferential access to some specific small scale or large scale magnetic structures.

In summary spatially resolved radio observations obtained at millimeter and decimeter-meter wavelength during the 1992 October 28 flare, support the idea that particle acceleration occurs at discrete sites, the locations of which vary with time in the primary energy release volume.

5. Conclusions

The 1992 October 28 flare is a relatively moderate one in terms of the amount of energy contained in both the thermal plasma (C2.6 GOES event) and the non-thermal electrons (a few 10^{29} ergs). Spatially resolved observations, available in the HXR, SXR, decimetric-metric and millimetric domains reveal however that the magnetic topology involved in the flare development is complex at all spatial scales. Stepwise temporal evolutions of the amount of energy release and of the efficiency of the non-thermal electron production are found to be related to similar stepwise variations of the magnetic structures at small and large scales illuminated by hot plasma or by non-thermal electrons.

– On the scale of the global loop structures revealed by soft X-ray emission, the present observations provide clear evidence for flare scenarios based on loop-loop interactions. Such a picture was already suggested by Heyvaerts et al. (1977), first confirmed by the SMM observations (see e.g. Hernandez et al. 1986; Machado et al. 1988) and supported by many YOHKOH observations (see e.g. Hanaoka 1997).
– At much smaller scales where energy release and particle acceleration take place, the radio observations provide strong support to the idea that these processes are highly fragmented in space and time.

In conclusion, these results provide some pieces of information to study how the small scale processes leading to particle acceleration are incorporated in the global magnetic structure associated with the flaring region. Multi-wavelength analysis of impulsive flares, such as the one performed in this paper, provide thus a powerful mean to investigate this problem which is one of the most critical issues for understanding particle acceleration (Miller et al. 1997) and for setting a realistic acceleration model.

Acknowledgements. The authors would like to acknowledge K.L. Klein for useful discussions and the anonymous referee for his constructive comments. This research work has been done with the financial support of the Fundação de Amparo a Pesquisa do Estado de São Paulo (FAPESP. Brazil) through contracts 96/06956-1 and 97/01869-6, the Conselho Nacional de Desenvolvimento Cientifico e Tecnologico (CNPq, Brazil) and Centre National de la Recherche Scientifique (CNRS, France), through the French-Brazilian cooperation program No 910172/96-0. NN would like to thank the NASA contract NAS 8-40801.

References

Antonucci E., 1994, Space Sci. Rev. 70, 149
Antonucci E., Alexander D., Culhane J.L., et al., 1999, In: Strong K.S., Saba J.L.R., Haisch B.M., Schmelz J.T. (eds.) The Many Faces of the Sun: A Summary of the Results from NASA's Solar Maximum Mission, ch. 10
Aschwanden M.J., Schwartz R.A., Alt D.M., 1995, ApJ 447, 923
Benz A.O., Barrow C.H., Dennis B.R., et al., 1983, Sol. Phys. 104, 179
Brown J.C., 1971, Sol. Phys. 18, 489
Chupp E.L., Trottet G., Marschhäuser H., et al., 1993, A&A 275, 602
Correia E., Costa J.E.R., Kaufmann P., Magun A., Herrmann, R., 1995, Sol. Phys. 159, 143
Costa J.E.R., Correia E., Kaufmann P., Magun, A., Hermann, R., 1995, Sol. Phys. 159, 157
Crosby N.B., Aschwanden M.J., Dennis B.R., 1993, Sol. Phys. 143, 275
Doschek G.A., Antiochos S.K., Antonucci E., et al., 1986, In: Kundu M.R., Woodgate B. (eds.) Proc. SMM Workshop, Energetic Phenomena on the Sun, ch. 4
Doschek G.A. 1990, ApJS 73, 117
Fisher G.H., Canfield R.C., McClymont A.N., 1985, ApJ 289, 425
Fisher G.H., 1989, ApJ 346, 1019
Giménez de Castro C.G., Raulin J.-P., Makhmutov V.S., Kaufmann P., Costa J.E.R, 1999, A&A (in press)
Georges C.B., Schaal R., Costa J.E.R., Kaufmann P., Magun A., 1989, In: SBMO-International Microwave Symposium/Brazil IEEE catalog No 89th0260-0, Vol. II, 447
Hanaoka Y., 1994, ApJ 420, L37
Hanaoka Y., 1997, Sol. Phys. 173, 319
Herrmann R., Magun A., Costa J.E.R., Correia E., Kaufmann P., 1992, Sol. Phys. 142, 157
Hernandez A.M., Machado M.E., Vilmer N., Trottet G., 1986, A&A 167, 77
Heyvaerts J., Priest E.R., Rust D.M., 1977, ApJ 216, 123
Hirayama T., 1974, Sol. Phys. 34, 323
Hurley K., Niel M., Talon R., Estulin I.V., Dolidze V.C., 1983, ApJ 265, 1076
Inda-Koide M., 1994, In: Enome S., Hirayama T. (eds.) Proc. of Kofu Symposium, NRO Report No 360, p. 161
Kaufmann P., Strauss F.M., Opher R., Laporte C., 1980, A&A 87, 58
Kaufmann P., 1985, Sol. Phys. 102, 97
Kiplinger A.L., Dennis B.R., Emslie A.G., Frost K.J., Orwig L.E., 1983, ApJ 265, L99
Kopp R.A., Pneumann G.W., 1976, Sol. Phys. 50, 85
Kosugi T., Makishima K., Murakami T., et al., 1991, Sol. Phys. 136, 17
Lu E.T., Hamilton R.J., McTiernan J.M., et al., 1993, ApJ 412 841
Machado M.E., Moore R.L., Hernandez A., et al., 1988, ApJ 326, 425
Manoharan P.K., van Driel-Gesztelyi L., Pick M., Démoulin P., 1996, ApJ 468, L73
Miller J.A., Cargill P.J., Emslie G.A., et al., 1997, JGR 102, 14631
Nishio M., Yaji K., Kosugi T., Nakajima H., Sakurai T., 1997, ApJ 489, 976
Raoult A., Pick M., Dennis B.R., Kane S.R., 1985, ApJ 299, 1027
Raulin J.-P., Kaufmann P., Olivieri R., et al., 1998, ApJ 498, L173
Sakao T., 1994, PhD Thesis, University of Tokyo
Sato J., Kosugi T., Makishima K., 1999, PASJ 51 127
Sturrock P.A., 1966, Nature 5050, 695
The Radioheliograph Group 1993, Adv. Space Res. 13, 9, 411
Trottet G., 1986, Sol. Phys. 104, 145
Trottet G., 1994, In: van den Oord G.H.J. (ed.) Fragmented Energy Release in Sun and Stars, Space Sci. Rev. 68, 149
Trottet G., Chupp E.L., Marschhäuser H., et al., 1994, A&A 288, 647
Trottet G., Vilmer N., Barat C., et al., 1998, A&A 334, 1099
Tsuneta S., Acton L., Bruner M., et al., 1991, Sol. Phys. 136, 37
Vilmer N., Trottet G., Barat C., et al., 1995, Space Sci. Rev. 68, 233
Vlahos L., 1994, Space Sci. Rev. 68, 39
Yoshimori M., Okudaira K., Hirasima Y., et al., 1991, Sol. Phys. 136, 347